Technical Physics, 2025, Vol. 70, No. 4

05

Effect of annealing on the high-strain-rate deformation of copper in Taylor tests

© E.S. Rodionov, A.E. Mayer, V.G. Lupanov, V.V. Pogorelko, P.N. Mayer, Yu.A. Lupitskaya, A.G. Fazlitdinova

Chelyabinsk State University,
454001 Chelyabinsk, Russia
e-mail: rodionoves.pgd@gmail.com

Received September 20, 2024
Revised November 19, 2024
Accepted November 20, 2024

The results of high-velocity impact experiments with cylindrical and profiled samples made of soft annealed copper with impact velocities up to 103−112 m/s are presented in comparison with previous results for hard cold-rolled copper. 3D numerical simulations of the experiments are performed based on the dislocation plasticity model numerically implemented by the method of smoothed particle hydrodynamics (SPH). It is shown that the dislocation plasticity model, which was previously parameterized using machine learning methods for hard cold-rolled copper, can successfully describe the deformation behavior of soft annealed copper when only the initial dislocation density changes to the level typical for annealed metals. At the same time, the shape of the deformed samples and the deformation behavior of cold-rolled and annealed samples differ significantly. It is shown that the proposed model adequately describes the grain refinement as a result of the dynamic deformation.

Keywords: dynamic deformation, dislocation plasticity model, material microstructure, deformation behavior, dislocation density.

DOI: 10.61011/TP.2025.04.61209.276-24

Introduction

Because of rapid expansion and deployment of new technologies the development of „digital twins“ that allow improving the products' and process parameters on tight schedule is now a pivotal issue. Among the key elements of the digital twins is that they provide reliable and credible data on the deformation properties of materials and structures, especially in case of intensive dynamic loads. The issues of dynamic loading of materials are relevant for many industries, including aircraft construction, military industry, design and protection of spacecraft, transport engineering, high-speed and precision machining. Recently, there has been the need for the development of domestic software systems in this area. In order for domestic software systems not only to simulate their foreign counterparts, but to outpace them, they shall be based on more accurate material models with greater predictive capacity.

Currently, in engineering practice, as well as in commercial finite element modeling packages, empirical models of plasticity are predominant for describing the deformation patterns, where the yield strength is set as an analytical function of deformation, strain rate, and temperature. Among the examples of such models are Johnson–Cook [1,2], Zerilli–Armstrong [3,4] and Preston-Tonks-Wallace models [5]. Johnson–Cook model became the most commonly used model. Empirical models are characterized by low computational costs and acceptable accuracy, however, they cannot predict the dependence of deformation behavior on the initial microstructure, microstructure changes during deformation, as well as specifics of the high-speed plastic relaxation, such as stress peaks in elastic shock wave precursors [6]. Non-ferrous metals may serve as an example because their mechanical properties are crucially impacted not only by the alloy's chemical composition, but also by the initial state of the alloy (hard, soft or semi-hard) obtained during preliminary thermomechanical treatment. The key difference of such states from each other is the internal microstructure of the material, characterized by differences in the density of defects, including the density of dislocations and grain boundaries. In the case of empirical plasticity models, when the initial state of the metal changes (after annealing, quenching, broaching, aging, etc.), it becomes necessary to redefine the coefficients of the model. Such problems arise also when describing the material repeated deformation.

Dislocation-based plasticity models with explicit description of the evolution of dislocation assembly during deformation [7–13] provide a more accurate and complete description of the process, including changes in the microstructure of the sample during deformation. In comparison with empirical models, the dislocation-based plasticity models have a more complex mathematical apparatus, which leads to a some increase in computation time, but they can operate in a wider range of the strain rates (up to $10^9\,\mathrm{s}^{-1}$ and above). Dislocation models allow us to take into account the evolution of mobile and immobile dislocation groups, including reproduction, annihilation, capture of dislocations into clusters (immobilization), as well as homogeneous nucleation, essential for ultra-high deformation rates [14,15]. The use of dislocation-based models allows avoiding the repeated parameterization when the initial state of the material changes: it will be enough to choose the correct initial defect density, which will be illustrated in this paper.

Search of optimal parameters is an essential issue for use of that or another model of the material. Empirical models are generally more easy in parametrization since they have less amount of parameters. On the other hand, active development of machine learning methods and their application to find optimal parameters [16–22] for material models makes optimization of multiparametric models more accessible. The results of experiments on high-strain-rate deformation can be used as a set of training data [17,19,23]. Currently, there's a vast diversity of experimental methods to study the metal properties in the wide range of deformation rates from the quasistatic loads to the ultra-high deformation rates reaching $10^9\,\mathrm{s}^{-1}$. Hopkinson–Kolsky bars are used to study the strain rates under $10^4\,\mathrm{s}^{-1}$ [24–26]; by comparing the incident, passed and reflected stress waves it is possible to plot the stress–strain curves. Substantial contribution to the study of dynamic properties is made by experiments on generation of plane shock waves in metals, where well-controlled dynamic loading conditions are provided for experimental measurement of dynamic yield stress and spallation strength [27,28] through interpreting the free surface velocity data recorded using laser interferometry [29]. Various plane shock waves generation methods allow covering a wider range of strain rates; for instance, the plates collision experiments [30–33] provide the shock-wave loading with the strain rates from 10^4 to $10^6\,\mathrm{s}^{-1}$ depending on the sample thickness. The strain rates about $10^6\,\mathrm{s}^{-1}$ and higher may be achieved in the shock waves generated through high-current electron irradiation [34,35] or powerful ion irradiation [36,37]. Due to the intensive laser pulses of short [38,39] and ultra-short duration [40–42] the steep fronts of shock waves with the strain rates up to $10^7-10^9\,\mathrm{s}^{-1}$ may be generated in the thin samples. The simplest implementation among other dynamic testing methods is the Taylor test [13,19,43–46], which assumes high-speed collision of cylindrical samples of the studied materials with a rigid barrier. This method combines high rates of deformation up to $10^5\,\mathrm{s}^{-1}$ and degrees of deformation of the order of units, but leads to inhomogeneous deformation over the sample volume, which makes it difficult to interpret the results. On the other hand, the use of machine learning methods makes it possible to effectively parameterize material models based on data from Taylor tests [18,19].

The aim of this paper is to further develop the dislocation plasticity model [12] and its numerical implementation for a three-dimensional case [13]. The main issue is whether this model may be extended to other initial microstructural states. To answer this question, an experimental and theoretical study of the deformation of soft annealed copper impactors was carried out and compared with the results of previous study [19], where parameterization of the dislocation plasticity model for hard cold-rolled copper was performed using machine learning methods. Experiments have been conducted on collisions of conventional and profiled samples with velocities of up to $103-112$ m/s (depending on the impactor shape). Profiling of samples in the head allows increasing the strain rates to a value of $10^5\,\mathrm{s}^{-1}$ already at a collision velocity of 100 m/s [19]. The results of experiments and microstructural analysis of annealed samples in comparison with the case of cold-rolled copper are described. The dislocation plasticity model [12] was used for numerical modeling, taking into account the kinetics of dislocations, supplemented by a grain size variation sub-model [19]. The dislocation plasticity model has been numerically implemented in the three-dimensional formulation [13] using the method of smoothed particle hydrodynamics (SPH) [47–49]. It is shown that a dislocation-based plasticity model parameterized in [19] for hard cold-rolled copper can successfully describe the deformation behavior of soft annealed copper when only the initial dislocation density is changed to the level typical for annealed metals. At the same time, the shape of the deformed samples and the deformation pattern of cold-rolled and annealed samples differ significantly. Section 1 describes the method of experiment and obtained results. Section 2 outlines the dislocation model of plasticity and its numerical implementation. Section 3 gives the results of computation compared to the experimental data.

1. Experimental study of annealed copper impactors

1.1. Experimental setup and samples

The samples are thrown with compressed air using a modified shock pipe (Fig. 1). A polypropylene guide tube with a length of 2.1 m and an inner diameter of 12 mm is placed inside the metal shock tube where the impactor moves. A stainless steel anvil is installed near the edge of the polypropylene pipe, which is also located inside the metal shock tube. During the experiment, the working part of the polypropylene pipe and the anvil are shielded by the metal body of the shock tube, providing additional protection. A high-pressure chamber (pumping chamber) is attached to the outer edge of the metallic shock tube. Maximal pressure in the pumping chamber makes 10 bar. When the membrane is punctured or ruptured, compressed air goes directly to the polypropylene pipe via an adapter sleeve. Inside the working part of the shock tube pressure is 0.05 bar, which significantly reduces the air resistance that occurs during the impactor acceleration, increasing the collision velocity. A polypropylene film was used as a membrane. To prevent the compressed gas from flowing into the area in front of the sample, the impactor is placed in a soft rubber or silicone shell. The sample and shell are lubricated with WD-40 silicone grease, which reduces friction during acceleration of the impactor and provides high collision velocity. The sample velocity is measured by the time-of-flight method with a base of 50 mm; the signal is a break in the conductive filament (solder).

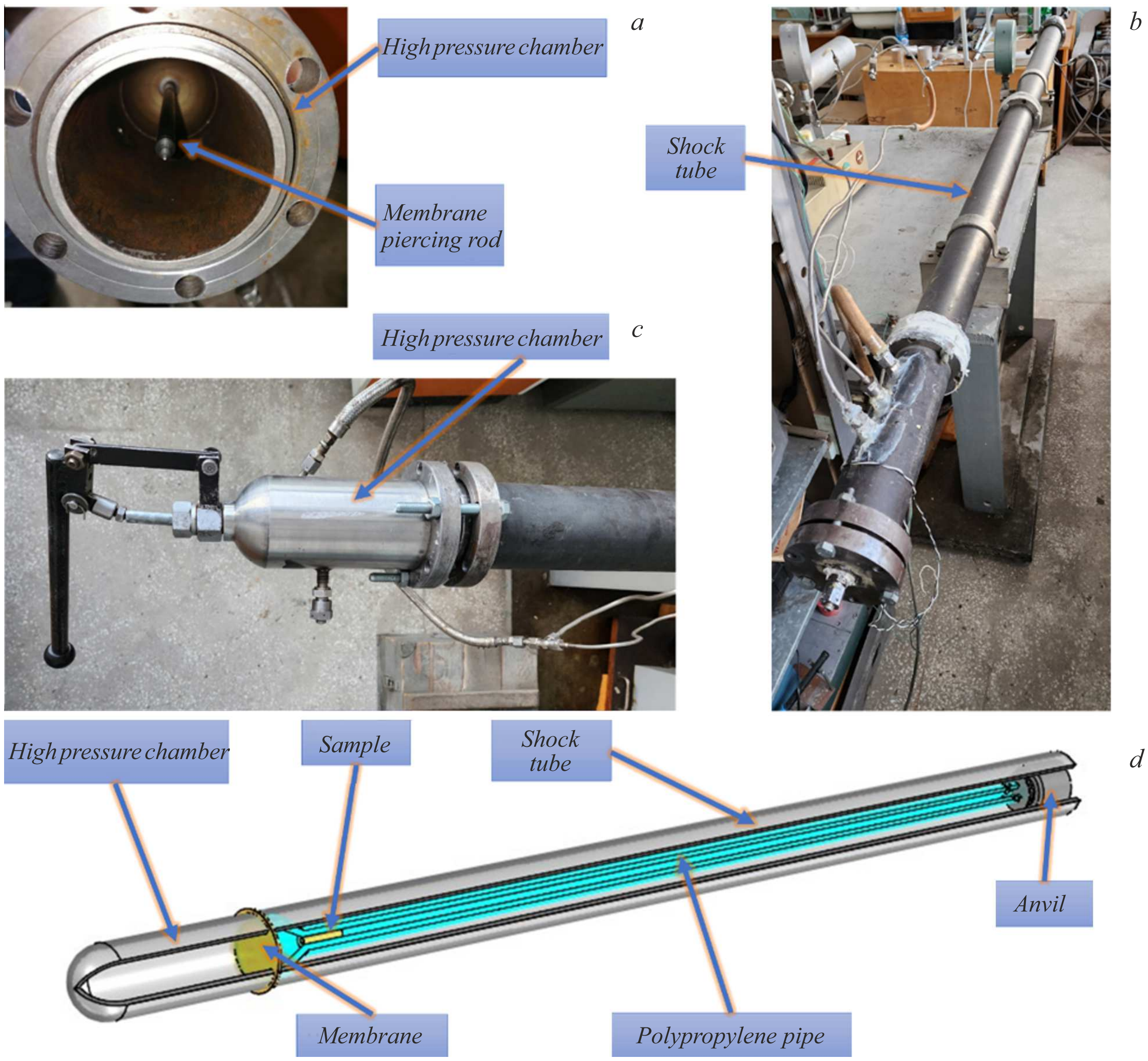

Figure 1. Photo and schematic representation of the shock tube modified for dynamic testing; *a* — high pressure chamber, interior view; *b* — shock tube assembly; *c* — high pressure chamber; *d* — schematic representation of the shock tube.

Annealed copper samples were used for dynamic testing. Cold-rolled copper M1T with impurities of no more than 0.1% was used as a base metal. The samples were annealed in a muffle furnace at a temperature of 900°C for 2 h, then, the samples and the furnace were cooled down to a room temperature (complete annealing). Annealing was carried out in the air, so slag appears on the surface of copper samples after annealing, which is easily removed from the metal surface. Annealed samples after slag removal are on average 0.5 mm shorter in length and diameter compared to the cold-rolled copper samples. Both conventional cylinders and profiled samples proposed in paper [19] were subjected to heat treatment. The profiling of the cylinders in the head makes it possible to reduce the diameter of the impact surface and achieve high strain rates and degrees of deformation of the material due to concentration of the impact energy. High-temperature annealing relieves mechanical stresses and reduces concentration of defects, thus, diminishing the strength and increasing the plasticity. A comparison of dynamically deformed annealed samples with cold-rolled copper, supplemented by microstructural analysis, makes it possible to show the effect of the same metal in different initial structural states on the plastic deformation process.

1.2. Results of dynamic tests

Samples geometry after annealing are given in Fig. 2. The experiments with conventional cylindrical samples with a pre-annealing diameter of 8 mm and pre-annealing length of

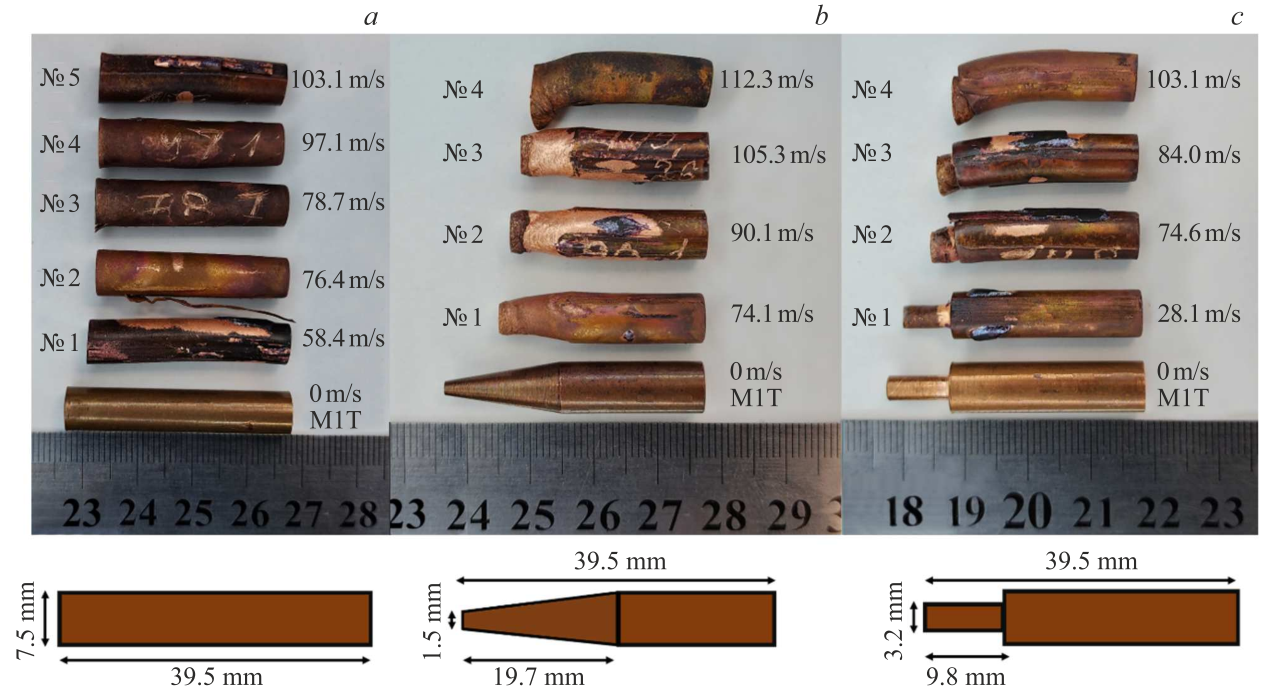

Figure 2. Photographs of copper samples after dynamic testing, as well as diagrams with geometry of annealed samples before dynamic deformation; *a* — conventional 8 mm cylinder; *b* — truncated cone; *c* — reduced 4-mm cylinder.

40 mm were carried out with collision velocities from 58.4 to 103.1 m/s (Fig. 2, *a*). For samples with truncated cone in the head the collision velocities were from 74.1 to 112.3 m/s (Fig. 2, *b*). For profiled samples with a head in the form of a reduced cylinder with a pre-annealing diameter of 4 mm and a pre-annealing length of 10 mm the experiments were carried out with impact velocities from 28.1 to 103.1m/s Previous computations [19] for the hard cold-rolled copper with collision velocities of 100–120 m/s provide strain rates varying from $10^4\,\mathrm{s}^{-1}$ for conventional cylinders to $10^5\,\mathrm{s}^{-1}$ for the truncated cone. Since the degree of deformation of annealed copper samples is higher, we can expect strain rates of at least the same order here at the maximum collision velocity studied.

The results of dynamic tests are shown in Fig. 2. The shape of annealed impactors compared with samples of cold-rolled copper from [19] is shown in Fig. 3. In case of a conventional 8-mm cylinder (Fig. 2, *a*, 3, *a*) at the collision velocities equivalent to experimental collision velocities of the cold-rolled copper M1T [19], a significant reduction of the sample length is observed. The diameter of the sample also increases along almost the entire length, but the flattening of the impact surface is less pronounced than in samples made of hard cold-rolled copper. Similar change in the deformation pattern is also observed for the profiled cylinders with conical (Fig. 2, *b*, 3, *b*) and reduced cylindrical (Fig. 2, *c*, 3, *c*) head. The deformation of the end section is achieved at lower collision velocities, which once again confirms the increased plasticity of the material.

The shape of the annealed profiled samples significantly loses its cylindrical symmetry after impact, and pronounced bending of the samples is observed (Fig. 2). At that, the cold-rolled samples tend to be less prone to bending (Fig. 3). In addition to the possible non-perpendicularity of the collision, there are fundamental reasons of why the deformed samples are not symmetrical. As shown in Section 1.3, the initial grain size in the annealed sample is about 300 μm, i.e., in the head of the profiled impactors, the diameter makes about 5–10 grains. The anisotropy of individual grains leads to heterogeneity of material properties on spatial scales comparable to the head of the profiled sample. On the other hand, in cold-rolled copper, the grain size is only of the order of 20 μm, which ensures a large number of grains, and as a consequence, leads to sufficiently averaged material properties in the sample's head and uniform deformation. This conclusion is confirmed by the results of molecular dynamic modeling [50], which shows bending of the sample in a perfectly perpendicular collision due to the anisotropy of individual grains.

1.3. Results of microstructural studies of annealed copper samples

In paper [19] we studied the samples made of cold-rolled hard copper M1T. This material is distinguished by its manufacturing process consisting of pressing and subsequent drawing operations, which greatly affects the internal structure of the material. The grains in such metal are $(18 \pm 4)\,\mu$m in size and elongated in the rolling direction. Prior to the experimental studies, single pores and

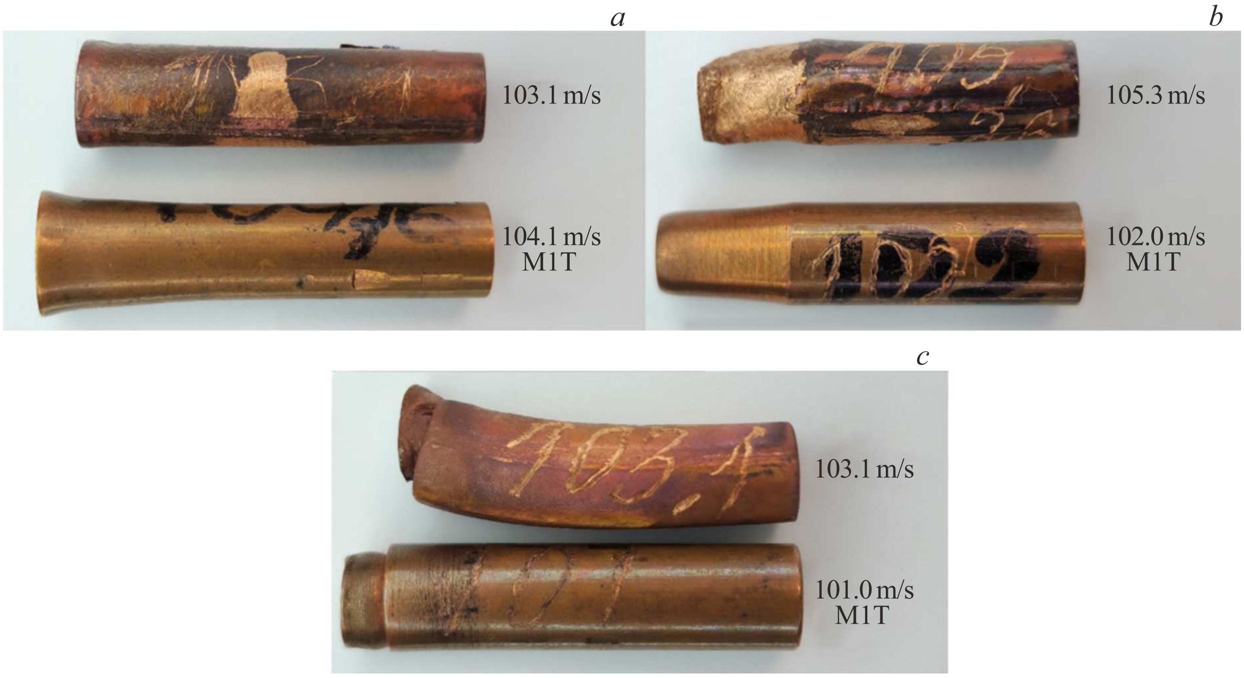

Figure 3. Deformed annealed copper impactors compared with results of the cold-rolled copper samples dynamic tests; *a* — conventional 8-mm cylinder; *b* — truncated cone; *c* — reduced 4-mm cylinder. Experiments for the hard cold-rolled copper from [19].

a large number of plastic deformation localization stripes in the rolling direction were observed in the samples (due to specifics of the material manufacturing process). Cracks of various sizes were observed in the deformed samples: small cracks were localized near the impact surface, and at the transition points of the profiled part of the cylinder to the main one, cracks spread over the entire diameter of the sample. A material with this structure is harder than hot-rolled copper, but it has lower strength properties, which is due to the initially high number of defects.

To relieve the residual stresses and ensure higher homogenization of the internal structure in order to increase the material ductility and improve its mechanical properties necessary for metallurgy, the heat treatment (annealing) of the material is used. The metal is placed inside a muffle furnace and heated to selected temperatures, aged, and then cooled in water or air. There are various kinds of metal heat treatment methods: for homogenization, recrystallization, complete annealing, etc. Complete annealing leads to recrystallization of the metal internal structure, triggering the loss of strength processes, and allows for getting a more homogeneous metal structure [51]. In this section, the internal structure of annealed copper will be considered in comparison with the structure of cold-rolled copper in its initial state before heat treatment.

Metallographic analysis was performed using METAM-LV optical microscope with a maximum magnification of 1000x. Conventional 8-mm diameter cylinders were used as samples: one sample was non-deformed, another one — dynamically impacted with a collision velocity of 76.4 m/s. The main goal was to study the initial microstructure and its changes during dynamic deformation. It is known that the initial microstructure of a material has a significant effect on its deformation and fracture [52]. A 3% solution of hydrogen peroxide, citric acid and salt (sodium chloride) was used for etching.

First, let's consider the non-deformed annealed sample (Fig. 4). No impurities were observed. The grain structure of the metal after etching may be observed with an unaided eye. The grain size of the non-deformed annealed sample is $(290 \pm 60)\,\mu$m, in the initial cold-rolled copper sample the grains were $(18 \pm 4)\,\mu$m in diameter [19]. Thus, after heat treatment, the linear grain size increased more than tenfold. After annealing, the grains that were stretched in the direction of rolling are not observed. The stripes of plastic flow localization completely disappeared in the annealed samples, and the diameter of the sub-grain structure increased to $9\,\mu$m versus $3\,\mu$m before annealing [19]. The sub-grain structure is mainly visible as a grid inside large grains. At the boundaries of the sample, the grain structure does not differ from the structure in the middle of the sample, unlike cold-rolled copper. In general, there are no any visible signs of the material pressing and rolling during its manufacture.

In a dynamically deformed sample (Fig. 5), a decrease in grain diameter to $(85 \pm 1)\,\mu$m is observed near the impact surface; in this area, a characteristic „grain cutting“ due to plastic deformation is observed. No any plastic flow

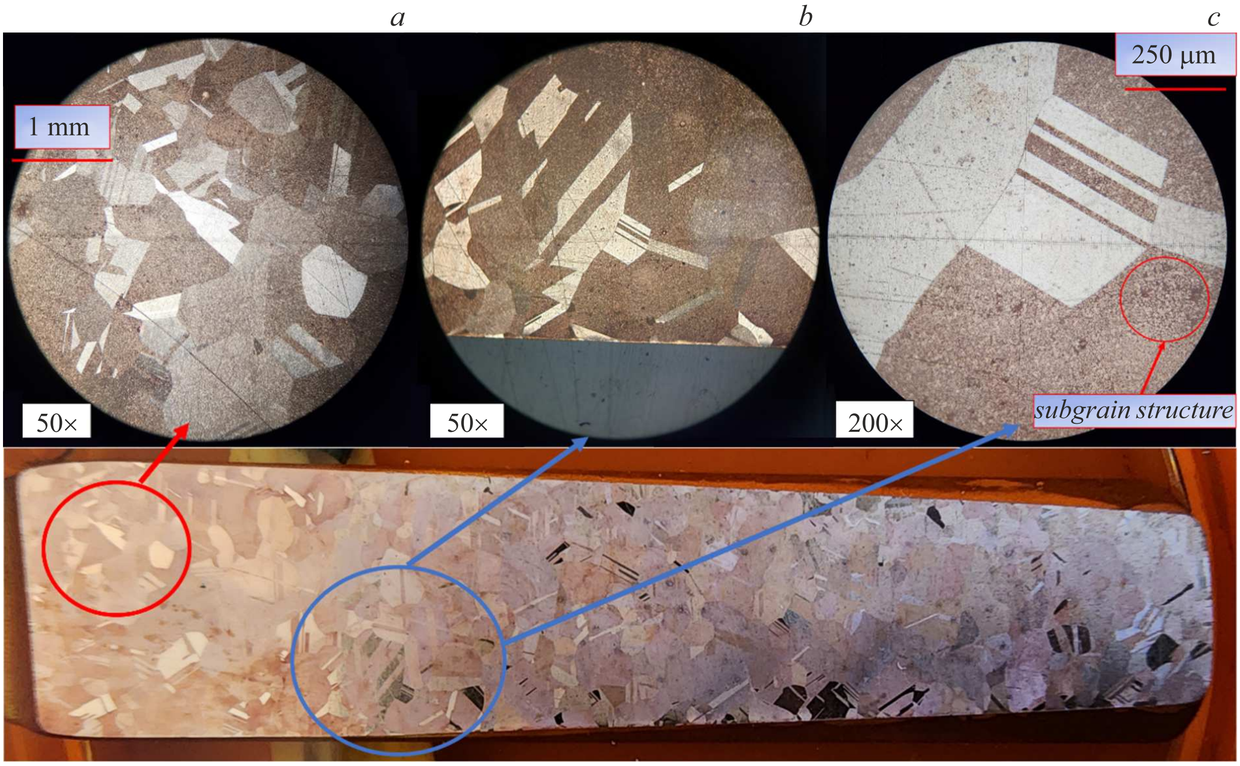

Figure 4. Optical micro-photos of a cross-section of the annealed copper sample obtained using a metallographic microscope; *a, b* — grain structure; *c* — sub-grain structure, size of sub-grains $9\,\mu$m.

localization stripes, porous structures and cracks specific for the cold-rolled copper [19] are observed. At the same time, a change in the size of the grain structure is observed along the entire length of the whole sample, in the rear part the grain size is $(150 \pm 40)\,\mu$m, which is less than in the non-deformed sample. It can be concluded that plastic deformation occurred along the entire length of the sample, varying the grain size to different extent. This type of grain grinding was not typical for cold-rolled copper samples. The change in structure correlates well with the results of experiments where the length of the heat-treated impactors was significantly reduced.

It follows from the results obtained that after dynamic tests, the structure of the heat-treated material and cold-rolled copper differs significantly. The annealed samples are more ductile. After heat treatment and dynamic testing, the impact surface is still more homogeneous in its structure than in cold-rolled samples, since pores and plastic deformation localization stripes do not appear. Grains in the impact plane are still visible by unaided eye, unlike cold-rolled samples, where the grain size on the impact surface can be estimated from above as less than $1\,\mu$m [19]. In heat-treated samples, after dynamic tests, a change in grain size is observed along the entire length of the impactor; in cold-rolled samples, the depth of visible structural changes at similar collision velocities was usually 3–6 mm.

2. Dislocation-based plasticity model and numerical implementation

Numerical modeling of experiments was carried out using a 3D implementation [13,19] of the dislocation-based plasticity model, that was first proposed in [11] and improved in [12] due to a more detailed description of kinetics with taking into account the immobilized dislocations. Within this model, the elastic portion of deformation is considered small, and the plastic portion of deformation is completely determined by the dislocations slipping along the crystal slip systems when impacted by mechanical stresses and the counteracting phonon friction, which is applicable for dynamic loading. The strain hardening is taken into account as a consequence of dislocations accumulated in the material. The model parameters are given in the Table below.

Conservation laws represent the core of continuum mechanics models [53] and define the evolution of density ρ, substance velocity $\mathbf{v}$ and specific internal energy E_Σ, that may be represented as a sum $E_\Sigma = E + E_S + E_D$, where E — the part related to the hydrostatic compression and heating, E_S — the part related to elastic modification of shape, and E_D — lattice (dislocations) defects energy. Conservation laws are expressed as follows:

$$\frac{d\rho}{dt} = -\rho(\nabla \cdot \mathbf{v}), \tag{1}$$

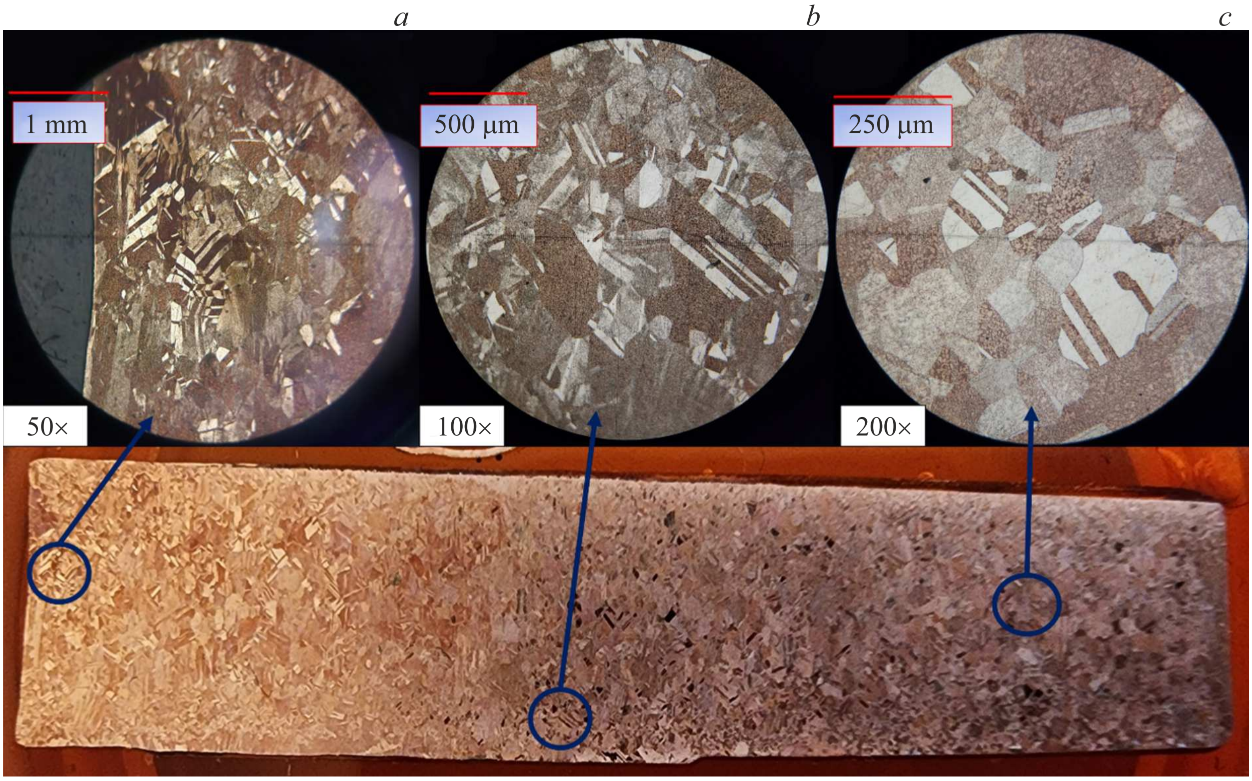

Figure 5. Optical micro-photos of the cross-section of a deformed annealed copper sample (8-mm cylinder, collision velocity of 76.4 m/s) made on a metallographic microscope; *a* — impact surface, *b* — central part of the sample; *c* — back part of the sample.

Parameters of dislocation plasticity model for annealed copper

Parameter	Value	Source
B, [Pa×s]	$0.45\cdot10^{-5}+2.5\cdot10^{-8}\times T$	[59,67]
μ	0.34	[12]
γ_{s0}, [MPa]	30	[12]
A_{I}	2.8	[19]
V_{I}, [m/s]	0.4	[19]
k_{D}, [J^{-1}]	$7.8\cdot10^{16}$	[12]
k_{A}	5	[12]
$\rho_{\mathrm{D}}^{\mathrm{free}}$, [m^{-2}]	10^{11}	[12]
$\rho_{\mathrm{D}}^{\delta}(t=0)$, [m^{-2}]	10^{11}	[12]
$\rho_{\mathrm{I}}^{\delta}(t=0)$, [m^{-2}]	10^{11}	–
β	0.9	[54]
ε_{D}, [eV/b]	8	[19]
γ_{GB}, [J/m^2]	0.5	[61–64]

Note. The hardening parameters are defined in [19] using machine learning methods.

$$\rho\,\frac{d\mathbf{v}}{dt}=(\nabla\cdot\boldsymbol{\sigma}),\tag{2}$$

$$\rho\,\frac{dE}{dt}=-P(\nabla\cdot\mathbf{v})+\beta(\mathbf{S}:\dot{\mathbf{w}}),\tag{3}$$

where total derivatives designate the rates of values transformation in the particles of the medium, $\boldsymbol{\sigma}=-P\mathbf{I}+\mathbf{S}$ — stress tensor, $P=P(\rho,e)$ — pressure found from the equation of state, and $\mathbf{S}$ — stress deviator; $\mathbf{I}$ — unit tensor. The last term on the right side of the equation (3) represents heating due to plastically dispersed mechanical energy, where $\dot{\mathbf{w}}$ — the rate of plastic deformation, $\beta=0.9$ — Taylor-Quinney coefficient [54].

The elastoplastic state is described by macroscopic strain tensor $\mathbf{u}$ and plastic deformation tensor $\mathbf{w}$. In case of small elastic deformations the difference $\mathbf{u}-\mathbf{w}$ may be used as the elastic deformations tensor. Stress deviators are calculated from Hooke's law [55]:

$$\mathbf{S}=2G\left[\mathbf{u}-\frac{1}{3}\,\mathrm{tr}(\mathbf{u})\mathbf{I}-\mathbf{w}\right],\tag{4}$$

where G — the shear modulus calculated similarly to [12] assuming the constant Poisson's ratio μ from the ratio $G=(3/2)\rho c_b^2(1-2\mu)(1+\mu)^{-1}$, where c_b — the volumetric speed of sound, determined from the equation of state for the current density and internal energy. The evolution of the macroscopic strain tensor is defined as follows:

$$\frac{d\mathbf{u}}{dt}=\frac{1}{2}\left[(\nabla\otimes\mathbf{v})+(\nabla\otimes\mathbf{v})^{\mathrm{T}}\right]+\left[(\mathbf{u}\cdot\dot{\mathbf{R}})+(\dot{\mathbf{R}}^{\mathrm{T}}\cdot\mathbf{u})\right],\tag{5}$$

where the rotation rate tensor $\dot{\mathbf{R}}=0.5[(\nabla\otimes\mathbf{v})-(\nabla\otimes\mathbf{v})^{\mathrm{T}}]$ represents the antisymmetric portion of the velocity gradient, upper index „T" denotes transposition, and symbol „$\otimes$" denotes dyadic product of tensors. The last term in equation

(5) takes into account the change in the components of the strain tensor due to the rotation of the elements of the medium in the laboratory coordinate system. The change in $\mathbf{w}$ is determined by both the rate of plastic deformation $\dot{\mathbf{w}}$ and rotation:

$$\frac{d\mathbf{w}}{dt} = \dot{\mathbf{w}} + \left[(\mathbf{w} \cdot \dot{\mathbf{R}}) + (\dot{\mathbf{R}}^{\mathrm{T}} \cdot \mathbf{w})\right]. \qquad (6)$$

Plasticity is provided by dislocation slipping and is described by the Orowan equation:

$$\dot{\mathbf{w}} = \sum_{\delta} \frac{1}{2}\left[(\mathbf{b}^{\delta} \otimes \mathbf{n}^{\delta}) + (\mathbf{b}^{\delta} \otimes \mathbf{n}^{\delta})^{\mathrm{T}}\right]\rho_{\mathrm{D}}^{\delta} V_{\mathrm{D}}^{\delta}, \qquad (7)$$

where index $\delta \in [1, 12]$ numerates the slip systems of FCC crystal [56], $\mathbf{b}^{\delta}$ — Burgers vector, $\mathbf{n}^{\delta}$ — normal line to the slip plane; $\rho_{\mathrm{D}}^{\delta}$ — scalar density of mobile dislocations and V_{D}^{δ} — dislocations slip velocity relative to the substance. When the elements of the medium are rotated during deformation, the components of the tensor $(\mathbf{b}^{\delta} \otimes \mathbf{n}^{\delta})$ are transformed similarly to the components of tensors $\mathbf{u}$ and $\mathbf{w}$ in equations (5) and (6), respectively, which allows for the change in orientation of the dislocations slip systems.

The effect of mechanical stress field on dislocations is described by the Peach-Koehler force per unit length of dislocation in the slip plane [54,57]:

$$F^{\delta} = \mathbf{b}^{\delta} \cdot \mathbf{S} \cdot \mathbf{n}^{\delta}. \qquad (8)$$

The balance of this force and the phonon friction force determines the sliding velocity of dislocations, which is calculated using a quasi-stationary analytical solution [58–60]:

$$V_{\mathrm{D}}^{\delta} = \frac{c_t \xi^{\delta}}{6\sqrt{6}\chi^{\delta}}\left[(\chi^{\delta})^{2/3} - 12\right]^{3/2}, \qquad (9)$$

$$\xi^{\delta} = \frac{1}{c_t B}\Big(F^{\delta} - \frac{bY_s}{2}\,\mathrm{sign}\,(F^{\delta})\Big) H\Big(|F^{\delta}| - \frac{bY_s}{2}\Big), \qquad (10)$$

$$\chi^{\delta} = 108|\xi^{\delta}| + 12\sqrt{3}\sqrt{4 + 27|\xi^{\delta}|^2}, \qquad (11)$$

where c_t — transverse sound speed, Y_s — static yield strength, $H(\bullet)$ — Heaviside function, $b = (2\sqrt{2})^{-1}\sqrt[3]{4m_1/\rho}$ — Burgers vector module, m_1 — mass of one atom.

Dislocation kinetics takes into account both mobile and immobile dislocations characterized by scalar densities $\rho_{\mathrm{D}}^{\delta}$ and $\rho_{\mathrm{I}}^{\delta}$, respectively. Mobile dislocations are understood as those that do not have strong stops and are able to move under the influence of applied shear stresses exceeding the static yield strength, see equations (9)–(11). Immobile dislocations are fixed by strong stoppers and do not participate in plastic stress relaxation, but provide strain hardening. Kinetics equations express the balance of multiplication velocities Q_{D}^{δ}, immobilization Q_{I}^{δ}, annihilation of mobile dislocations Q_{A}^{δ} and annihilation of mobile and immobile dislocations Q_{AI}^{δ} [12]:

$$\frac{d\rho_{\mathrm{D}}^{\delta}}{dt} = Q_{\mathrm{D}}^{\delta} - Q_{\mathrm{I}}^{\delta} - Q_{\mathrm{A}}^{\delta} - Q_{\mathrm{AI}}^{\delta} - \rho_{\mathrm{D}}^{\delta}(\nabla \cdot \mathbf{v}), \qquad (12)$$

$$\frac{d\rho_{\mathrm{I}}^{\delta}}{dt} = Q_{\mathrm{I}}^{\delta} - Q_{\mathrm{AI}}^{\delta} - \rho_{\mathrm{I}}^{\delta}(\nabla \cdot \mathbf{v}). \qquad (13)$$

The last terms on the right-hand side of equations (12) and (13) take into account the kinematic change in dislocation density due to compression or stretching of the substance. The energy approach proposed in [11] is used to calculate the dislocation multiplication rate:

$$Q_{\mathrm{D}}^{\delta} = k_{\mathrm{D}} b \rho_{\mathrm{D}}^{\delta} |F_{\mathrm{D}}^{\delta} V_{\mathrm{D}}^{\delta}|, \qquad (14)$$

where $k_{\mathrm{D}} = (1 - \beta)/(8\,\mathrm{eV})$ — generation coefficient. The immobilization rate may be written as follows [12]:

$$Q_{\mathrm{I}}^{\delta} = V_{\mathrm{I}}(\rho_{\mathrm{D}}^{\delta} - \rho_{\mathrm{D}}^{\mathrm{free}})\sqrt{\rho_{\mathrm{I}}^{\delta}}, \qquad (15)$$

where $\rho_{\mathrm{D}}^{\mathrm{free}}$ — threshold value for the start of immobilization, V_{I} — immobilization rate parameter. Annihilation rate is equal

$$Q_{\mathrm{A}}^{\delta} = 2k_{\mathrm{A}} b |V_{\mathrm{D}}^{\delta}| (\rho_{\mathrm{D}}^{\delta})^2, \;\; Q_{\mathrm{AI}}^{\delta} = k_{\mathrm{A}} b |V_{\mathrm{D}}^{\delta}| (\rho_{\mathrm{D}}^{\delta}\rho_{\mathrm{I}}^{\delta}), \qquad (16)$$

where k_{A} — annihilation coefficient. Strain hardening is delineated by Taylor law:

$$Y_s = Y_{s0} + \mathrm{A_I} G b \sqrt{\rho_{\mathrm{I}}}, \quad \rho_{\mathrm{I}} = \sum_{\delta} \rho_{\mathrm{I}}^{\delta}, \qquad (17)$$

where Y_{s0} — statistic yield strength in the dislocation-free material. In addition to the accumulation of dislocations, hardening can be associated with grain boundaries, which is usually taken into account by the Hall-Petch relation. On the other hand, for dynamic deformation, a significant contribution of this term can be expected at submicron grain sizes, which is a far cry from the considered grain size range.

In paper [19] additional equation is proposed to account for variation of the grain size d during the material deformation process:

$$d = \left[d_0^{-1} + \frac{1}{3\gamma_{\mathrm{GB}}}\int_0^t \prod dt'\right]^{-1}, \qquad (18)$$

where d_0 — initial grain size, $\gamma_{\mathrm{GB}} = 0.5\,\mathrm{m}^2$ — characteristic energy of the grains boundaries [61–64]. When deriving equation (14), it is assumed that the formation of new grain boundaries occurs due to the power released during the annihilation of dislocations:

$$\prod = \varepsilon_{\mathrm{D}} \sum_{\delta} (Q_{\mathrm{A}}^{\delta} + 2Q_{\mathrm{AI}}^{\delta}), \qquad (19)$$

where $\varepsilon_{\mathrm{D}} = 8\,\mathrm{eV}/b$ — energy of the dislocation line unit length.

The numerical implementation of the model for the three-dimensional case is described in [13]. The method of splitting by physical processes is used. SPH method (smoothed particle hydrodynamics) is used for computing the spatial gradients [48,49,65]. Within the framework of this approach, a continuous medium is divided into particles, and the mechanical characteristics of each particle are blurred using a smoothing kernel. Finding spatial derivatives is reduced to the analytical computation of the derivatives of the kernel function and summation over neighboring particles. The kinetics of dislocation plasticity is calculated independently in each particle of the medium. The time integration of the equations is performed by the explicit Eulerian method with a time step determined by the Courant condition. Artificial viscosity is used to stabilize solutions with sharp velocity gradients [48]. The equation of state of copper in the form of an artificial neural network is used for pressure computation [13]. The model parameters in the table are taken from the previous study [19] for hard cold-rolled copper, except for the initial density of immobile dislocations $\rho_{\mathrm{I}}^{\delta}(t=0)$, for which the characteristic value for annealed metals is used. The initial value of the density of mobile dislocations in every slip system $\rho_{\mathrm{D}}^{\delta}(t=0)$ is taken equal to the threshold for the onset of immobilization $\rho_{\mathrm{D}}^{\mathrm{free}}$, see equation (15).

The numerical solution in single-flow mode is implemented as SPHEP program in Fortran language [13]. The particles are initially placed in the nodes of the BCC lattice, which ensures their better connectivity compared to a simple lattice. The number of SPH-particles in the system makes from 39 000 to 55 000 depending on the impactor shape. Free boundary conditions were set on all surfaces of the impactor, except for contact with the anvil, for which the conditions of impermeability and free slipping are set. At the initial moment of time, all particles are given the same initial velocity towards the anvil. OVITO software is used to visualize the obtained results [66].

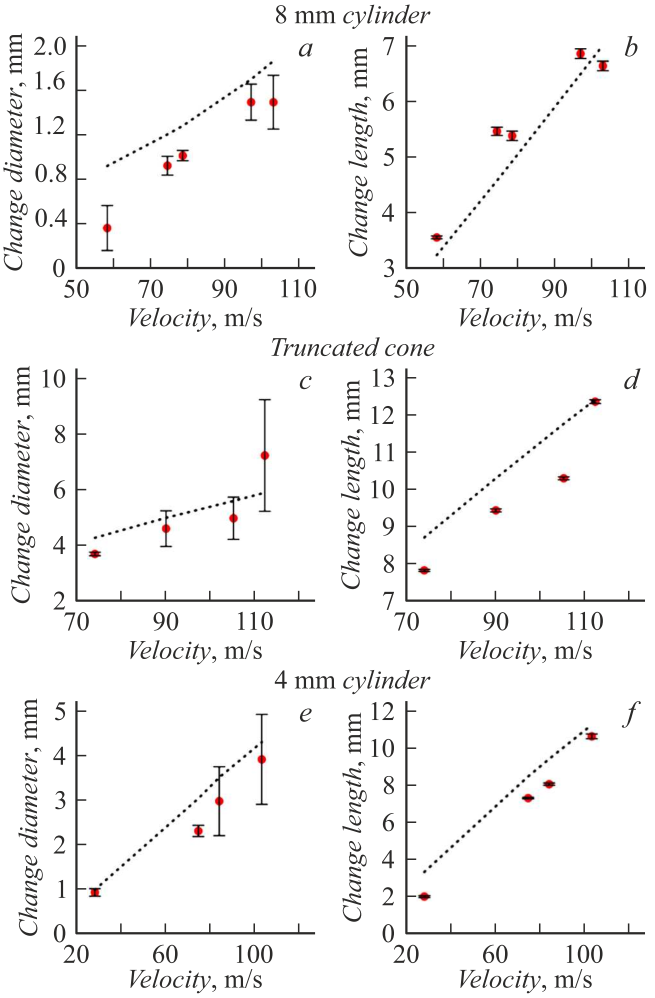

Figure 6. Computation results compared with experimental data for the annealed copper samples. Diameter changes (a, c, e) and length changes (b, d, f) versus impact velocity for a 8-mm conventional cylinder (a, b), truncated cone (c, d) and 4-mm profiled cylinder (e, f). The calculation results are represented by a black dotted line, and the experimental results are represented by circles with error intervals.

3. Modeling results

3.1. Comparison of computations and experiments for annealed copper

For non-annealed cold-rolled copper, optimization of model parameters using machine learning methods [19] led to an initial density of immobilized dislocations $\rho_{\mathrm{I}}^{\delta}(t=0)=6.3\cdot10^{12}\,\mathrm{m}^{-2}$, which in total over all slip planes gives $76\cdot10^{12}\,\mathrm{m}^{-2}$, corresponding to the case of strongly deformed metals. The large plastic deformation of the annealed samples and the results of their microstructural analysis show that annealing made the metal much more softer. Annealing reduces the defect concentration, and for annealed metals the characteristic dislocation density is of the order of $10^{12}\,\mathrm{m}^{-2}$. Therefore, in computations for the annealed samples the initial density of dislocations was taken equal $\rho_{\mathrm{I}}^{\delta}(t=0)=10^{11}\,\mathrm{m}^{-2}$, that in total for all slip planes gives a value of $1.2\cdot10^{12}\,\mathrm{m}^{-2}$. This change in the initial dislocation density can be considered physically justified. Note that the same reduced initial dislocation density was used in [19] when comparing computations with the shock wave experiments [68] performed on normalized samples. The remaining parameters of the dislocation-based plasticity model, in particular, the hardening coefficient A_{I} and the rate of dislocation immobilization V_{I}, remained the same as for cold-rolled copper in [19]. The absence of the need to parameterize the theoretical model when changing the internal structure of the material is a significant advantage of physically based plasticity models compared to empirical models.

Fig. 6 shows comparison of the modeling and experimental data. Changes in the length and diameter of the sample in the head as a result of the collision relative to their initial values were selected as geometry parameters for comparison. In case of an 8 mm conventional cylinder, the prediction of the model for changing the diameter of the head (Fig. 6, a) slightly exceeds the experimental values, but in absolute terms the error is only tenths of a millimeter. It is worth noting that there are experiments where the error in measuring the diameter of the head part of the profiled cylinders is quite large. This is due to the fact that after annealing, the grain size increases significantly. Therefore, the head of the annealed samples may contain only a few large grains. Such structure can lead to localization of plastic deformation at the grain boundaries, which can disrupt the cylindrical symmetry of the samples. As an example, the impact surface of a truncated cone is shown in Fig. 7, *d*. This phenomenon is less pronounced on conventional 8 mm samples, since a large number of grains are placed on the impact surface.

Fig. 7, *a*–*c* illustrates comparison of the shape of an experimental sample with SPH-analysis. In case of a conventional 8 mm cylinder (Fig. 7, *a*), the model well describes the increase in the diameter of the sample along almost its entire length. In the case of a 4 mm reduced cylinder (Fig. 7, *b*) and a truncated cone (Fig. 7, *c*), the results of numerical modeling predict the deformation of the non-profiled part of the cylinder, which corresponds to experimental data.

In general, the model that was previously parameterized for cold-rolled copper cylinders [19] describes the experimental results for annealed samples with good accuracy. To do this, it was necessary to change only one parameter of the model — initial density of immobilized dislocations, which is physically justified.

3.2. Dynamics of deformation based on SPH-computations

Comparison of the calculated sample shape with the experimental one for a uniform 8 mm cylinder is shown in Fig. 7, *a* and shows a rise in diameter along almost the entire length of the sample. Fig. 8, *a* illustrates equivalent plastic deformation w_M, which is a scalar measure of the plastic deformation tensor $\mathbf{w}$:

$$w_M = \sqrt{(2/3)(\mathbf{w} : \mathbf{w})}. \qquad (20)$$

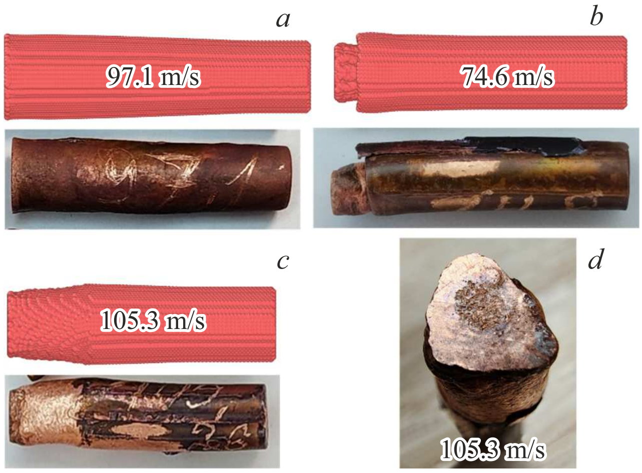

Figure 7. Final sample shapes after deformation compared for different impactor shapes: *a* — uniform 8 mm cylinder; *b* — reduced 4 mm cylinder; *c* — truncated cone; *d* — A photograph of the impact surface of a truncated cone with a clearly distorted axial symmetry is shown.

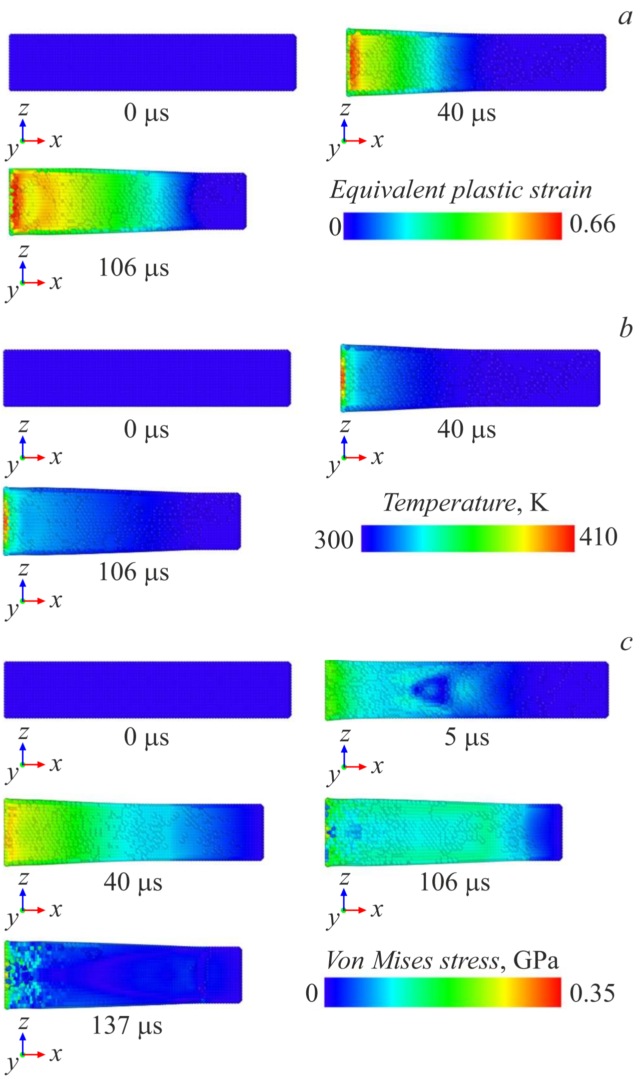

Figure 8. SPH-computations for conventional 8-mm cylinder (impact velocity 103.1 m/s); spatial distributions: *a* — equivalent plastic deformation, *b* — temperature; *c* — equivalent von Mises stress in central cross-section sequentially.

The plastic deformation is distributed practically over the entire length of the sample and decreases to zero only near the back surface. The highest values of plastic deformation are concentrated on the impact surface along almost the entire diameter of the sample, which correlates well with the results of microstructural analysis, where the greatest grain refinement was recorded on the impact surface of the sample.

Fig. 8, *b* shows temperature distribution in the numerical experiment. The highest temperatures are obtained in the central part of the impact surface of the sample. Maximal temperature rise makes about 110 K. Figure 8, *c* shows the spatial distribution of the equivalent von Mises stress σ_M,

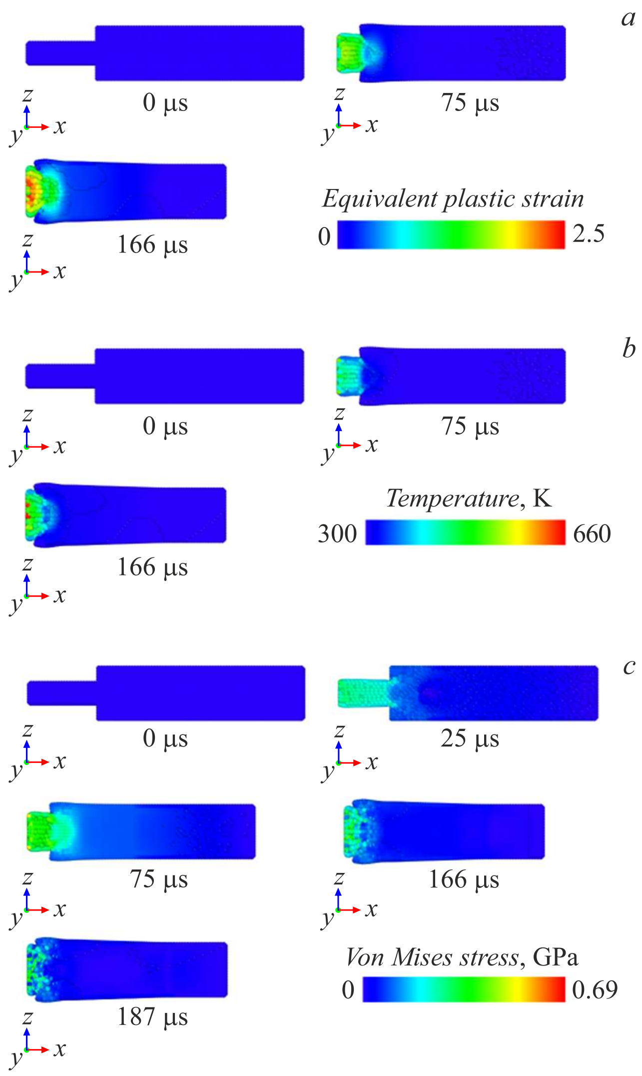

Figure 9. SPH-computations for the profiled 4-mm cylinder (impact velocity 103.1 m/s); spatial distributions: *a* — equivalent plastic deformation, *b* — temperature; *c* — equivalent von Mises stress in central cross-section sequentially.

which is a measure of the stress deviator **S**:

$$\sigma_M = \sqrt{(3/2)(\mathbf{S}:\mathbf{S})}. \qquad (21)$$

After the start of deformation, a uniform stress distribution is observed along almost the entire length of the sample with values of 0.16–0.18 GPa. The highest stresses are observed on the impact surface. After the sample is stopped and further rebound, a sharp drop in stress is observed.

Fig. 7, *b* shows a comparison of the shape of the experimental sample with the result of numerical analysis for a profiled sample with a cylinder head of a smaller radius. The simulation repeats the trend of a uniform increase in the diameter of the head of the impactor. The degree of diameter increase grows with increasing impact velocity. The modeling also well describes the velocity threshold at which the diameter of the main (end) part of the cylinder begins to increase. Fig. 9, *a, b* shows the spatial distribution of plastic deformation and similar temperature distribution. Plastic deformation is mainly concentrated in the head part, which corresponds to the assumption of [69], but it also extends deep into the main part of the sample. The highest values are observed on the impact surface. The highest temperature rise on the impact surface reaches 360 K. Average temperature in the head portion of the sample is about 380–400 K. Von Mises stress reaches about 0.7 GPa (Fig. 9, *c*). The average stress in the deformed part of the sample is 0.28–0.32 GPa. It is worth noting that the distribution of stresses and plastic deformation differs from the case of conventional 8 mm cylinder. This is due to a change in diameter during transition from the sample head to the main part, which affects the pattern of shock wave propagation in the sample.

For the case of cones, a comparison of the shapes of deformed samples is shown in Fig. 7, *c* and illustrates predominant flattening during the collision of the cone-shaped head. Fig. 10, *a* shows distribution of plastic deformation at successive time points. Plastic deformation affects the head part up to the transition to the end part of the sample. The temperature distribution is shown in Fig. 10, *b*. The temperature in the deformed region of the truncated cone averages 610–650 K, the maximum temperature is about 830 K, which is still far from the melting point of copper. The field of shear stresses is shown in Fig. 10, *c*. Maximum stress on the contact surface is about 1 GPa, the average for the sample head is about 0.4 GPa.

3.3. Comparison of dynamic deformation of soft and hard copper

To compare the spatial distribution of equivalent plastic deformation, temperature, and von Mises stresses with the case of cold-rolled copper samples, a series of calculations was performed for a conventional 8 mm cylinder, profiled 4 mm cylinder, and a truncated cone. The parameters of the dislocation-based plasticity model from [19] were used for cold-rolled samples. Initial geometry was taken equal for all samples. Each cylinder had initial velocity of 100 m/s. The distribution patterns were recorded at the moment when the impactor's back was stopped. Comparison of results is given in Fig. 11.

In the case of conventional 8-mm impactors (Fig. 11, *a*), annealed samples show a tendency to a greater decrease in length and a smaller increase in diameter compared with cold-rolled copper impactors. The diameter of annealed samples varies practically along the entire length of the sample, unlike cold-rolled copper impactors. The maximum values of plastic deformation, temperature, and stress are higher for a cold-rolled impactor. Plastic deformation in the annealed impactors tends to zero only near the back of the sample, while in the case of hard copper M1T it becomes zero for about 1/4 of the total length of the cylinder. The temperature distributions are similar to each other, with a maximum at the impact surface. The shear

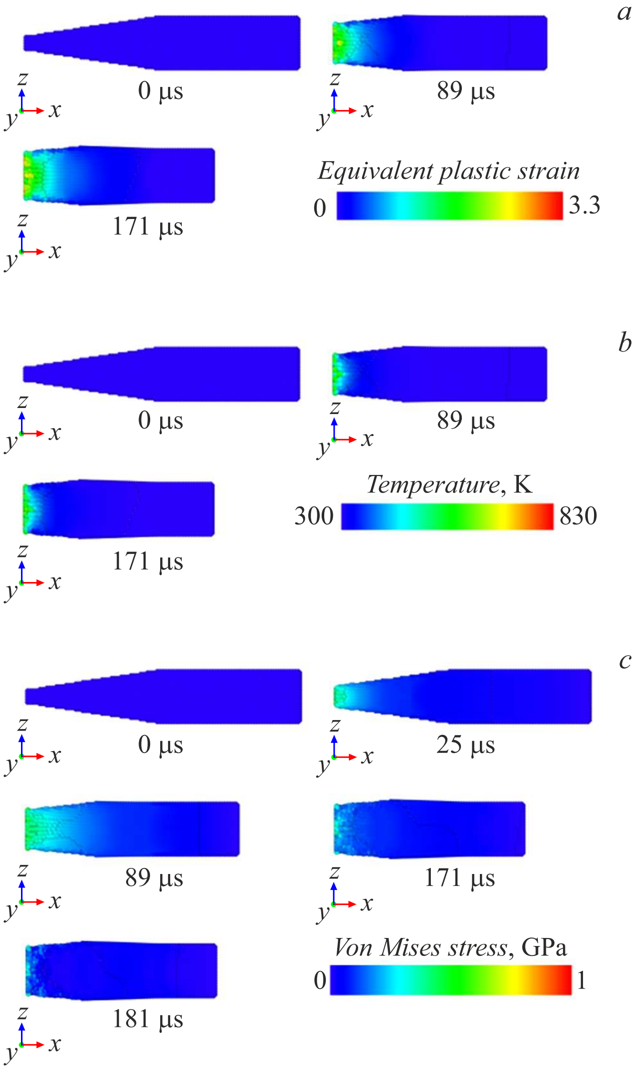

Figure 10. SPH-computations for the truncated cone in the head part (impact velocity 112.3 m/s); spatial distributions: *a* — equivalent plastic deformation, *b* — temperature and *c* — equivalent von Mises stress in central cross-section sequentially.

stress distributions are similar, but only the maximum and average values of these fields differ.

In case of profiled 4mm impactors (Fig. 11, *b*), as for conventional 8 mm cylinders, there is a tendency to reduced length of annealed samples compared to the cold-rolled ones. In case of annealed samples, deformation and increased diameter of the main, non-profiled part of the cylinder are observed; in samples made of cold-rolled copper, a similar effect is observed only at high impact velocities. In case of annealed samples, plastic deformation affects the main part of the cylinder, whereas in M1T copper impactors, plastic deformation in the main part of the cylinder is zero. Fig. 11, *c* illustrates distribution of plastic deformation, temperature and stresses for samples as a truncated cone. For annealed cone, there is a tendency to align the diameter of the impact surface and the main part of the cylinder. As for other forms of samples, plastic deformation is less localized near the impact surface in comparison with cold-rolled copper.

Figure 12 shows the dependences on the collision velocity of the normalized geometric dimensions of annealed copper samples in comparison with the results of [19] for cold-rolled copper. The numerical models for the two microstructural states differ only in the initial density of immobile dislocations, while the model correctly takes into account the tendency for a stronger increase in diameter and a decrease in length of annealed samples in comparison with cold-rolled hard copper samples. The same conclusion is confirmed by Fig. 13, which shows a comparison of the shape of the annealed copper samples after collision with the experimental and calculated results from paper [19] for the cold-rolled copper samples. Since the parameterization of the model for annealed copper was not carried out, and the value of the initial dislocation density was taken from physical considerations as a characteristic value for annealed metal, the results obtained can be considered a verification of the model.

Figure 14 shows a comparison of the final total dislocation density in samples of soft annealed and hard cold-rolled copper. In annealed copper with low initial dislocation density, plastic deformation leads to a monotonous increase in dislocation density and strain hardening (and an increase in the static yield strength (see equation (17))). Upon collision, as the plastic deformation spreads along the length of the annealed sample, hardened material layers are generated in it, which are further harder to deform compared to adjacent layers that have not yet been hardened. As a result, plastic deformation is moved further away from the collision surface. In cold-rolled copper, the initial dislocation density is already very high, and dynamic deformation at the initial stages leads to a decrease in dislocation density and softening of the material. This is due to annihilation of mobile dislocations generated by plastic deformation with the immobile ones; similar processes of decreasing dislocation density after peak values are observed in molecular dynamic modeling [70]. Fig. 14 shows that the cold-rolled samples contain a region of reduced dislocation density compared to the initial state. Such softening of the material leads to localization of plastic deformation in the head of the sample. This explains the difference in the deformation pattern between the annealed and cold-rolled samples. It should be noted that further deformation leads to an increase in the dislocation density near the impact surface to a level higher than the initial one (Fig. 14, *d–f*); thus, softening in cold-rolled samples is replaced by hardening.

3.4. Strain–stress curves

In the mechanics of a deformable solid, an important aspect is the analysis of stress-strain curves. Using the dislocation plasticity model, we calculated such curves for a given uniform external deformation. Figure 15 shows the true stress versus true strain curves for the soft annealed

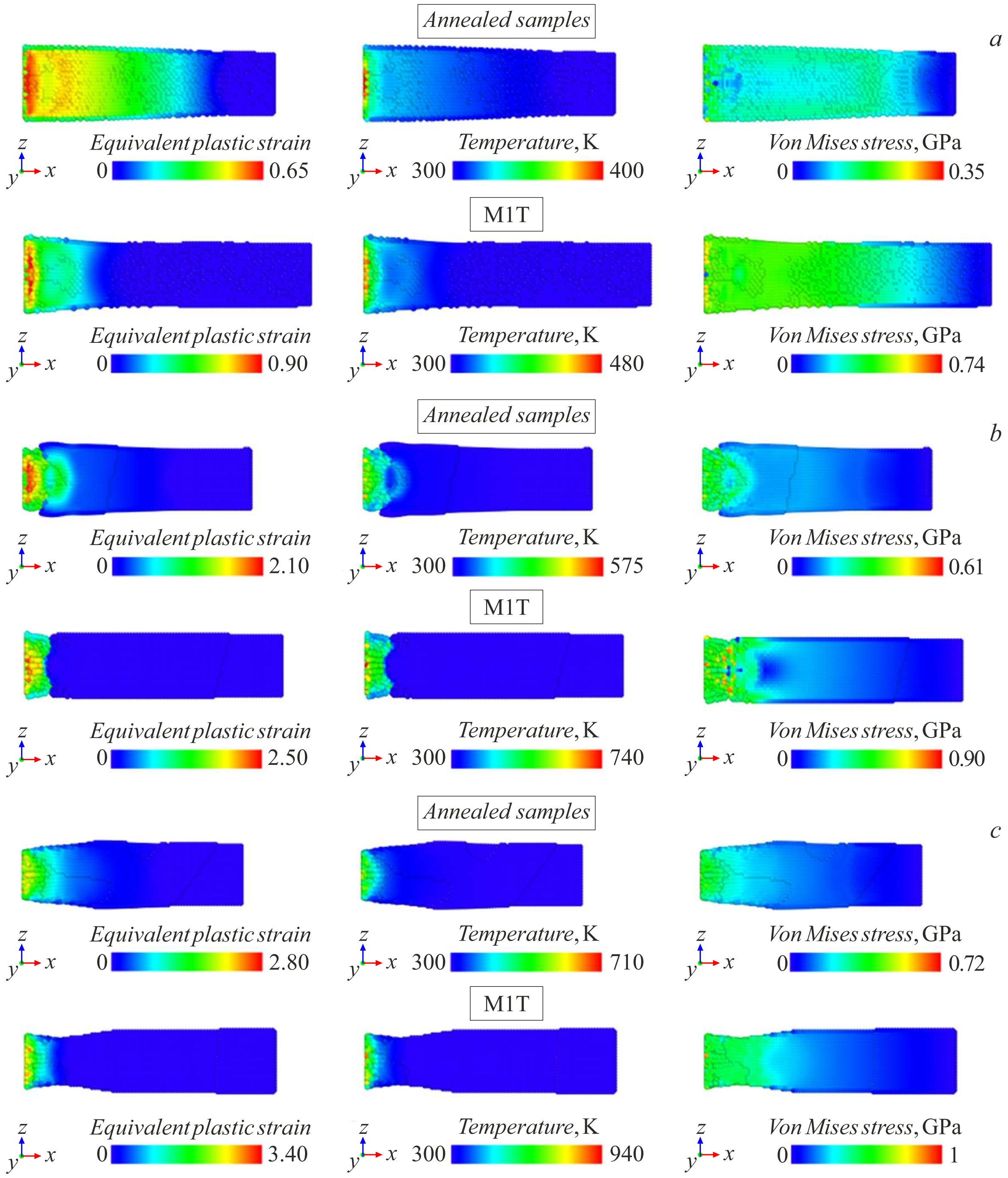

Figure 11. Spatial distribution of plastic deformation, temperature, and von Mises stresses for samples of soft annealed and hard cold-rolled copper for different shapes of impactors: *a* — conventional 8-mm cylinder, *b* — profiled 4-mm cylinder, *c* — truncated cone.

and hard cold-rolled copper, calculated for simple stretching (uniaxial stress state) at different rates of deformation. In the first case the initial density of immobile dislocations makes $1.2 \cdot 10^{12}\,\mathrm{m}^{-2}$, and in the second case — $76 \cdot 10^{12}\,\mathrm{m}^{-2}$. In the initial section of the curve for high strain rates, there is a stress spike (yield drop) associated with a temporary shortage of mobile dislocations for stress relaxation. Further, for annealed copper, a monotonous hardening is observed, associated with the accumulation of immobile dislocations. At the same time, the dependence of the yield strength on the strain rate at deformation of more than 0.03 is non-monotonic because immobilization of dislocations into dislocation structures has a finite rate. For the cold-rolled copper at the deformation rate of $10^4\,\mathrm{s}^{-1}$ and less the stresses quickly go to an almost constant level. This behavior qualitatively coincides with the experimental stress-strain curves [71]; a quantitative coincidence with the stress level of about 350 MPa occurs for the intermediate value of

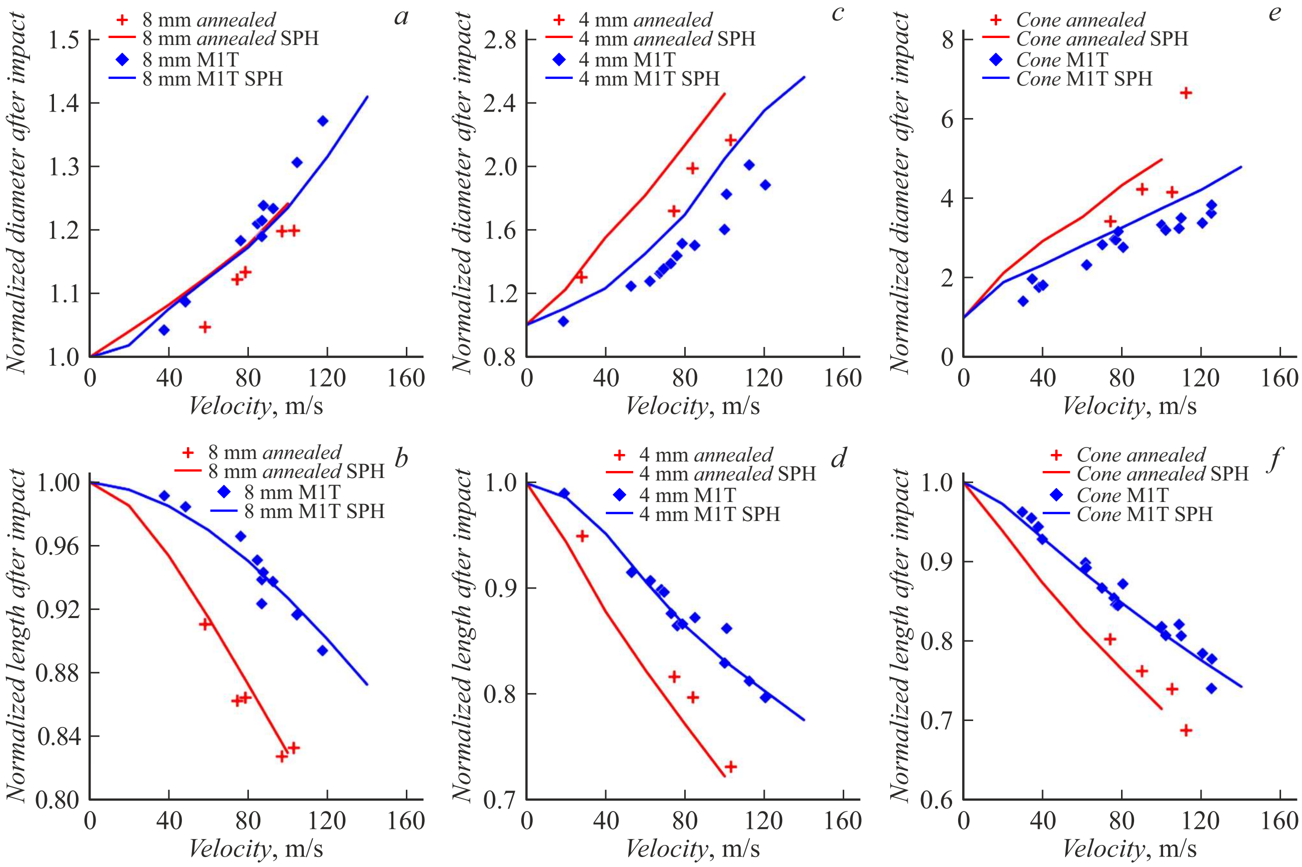

Figure 12. Comparison of experimental results (markers) and calculations (lines) for cold-rolled and annealed samples in the case of *a, b* — conventional 8-mm cylinders, *c, d* — profiled 4-mm cylinders and *e, f* — truncated cones: *a, c, e* — normalized to the initial diameter of the impact surface of the sample after impact, *b, d, f* — normalized to the initial length sample after impact. For the cold-rolled copper samples the results are provided in [19].

initial density of immobile dislocations of $24 \cdot 10^{12}\,\mathrm{m}^{-2}$. At high strain rates, a yield drop is observed, similar to annealed copper. After the initial set interval, the stresses in cold-rolled copper are maintained in a narrower range than for annealed copper. In this case, both hardening and softening of cold-rolled copper can be observed due to the mutual annihilation of mobile and immobile dislocations, which was discussed earlier. The experimental results from [72] show higher values of flow stresses from 300 to 450 MPa with a decrease in the average grain size from 315 to $9.5\,\mu$m, which is less than the calculated difference in flow stresses between the annealed and cold-rolled copper with a comparable difference in grains sizes (Fig. 15). On the other hand, strength significantly depends on the density of dislocations, and not only on the grain size. In addition, the specific setting of the experiment and the stress state in the sample are important.

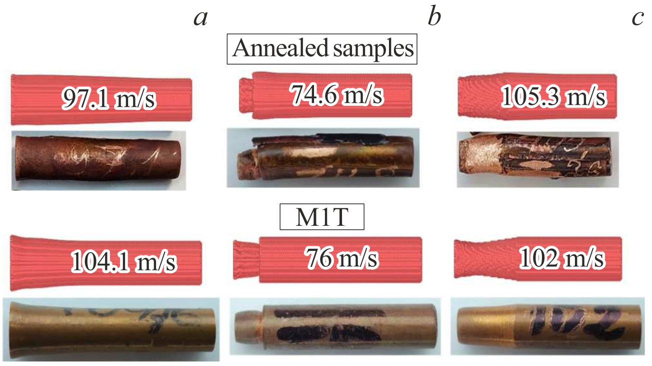

Figure 13. Comparison of experimental and calculated shapes of cold-rolled (bottom row) copper samples from [19] and annealed (top row) copper for: *a* — conventional 8-mm cylinders, *b* — profiled 4-mm cylinders, *c* — truncated cones. Results are provided for close collision velocities.

3.5. Evaluation of grain refinement

For annealed copper samples, the grain structure refinement was evaluated using equation (18). Variation of the grain size in theoretical model and in experiment compared is shown in Fig. 16. The initial diameter $d_0 = d(t = 0) \approx 290\,\mu$m is taken from the experimental data for the initial material. The grain refinement model proposed in [19] has good accuracy in description of the grains size near the impact surface. The numerical

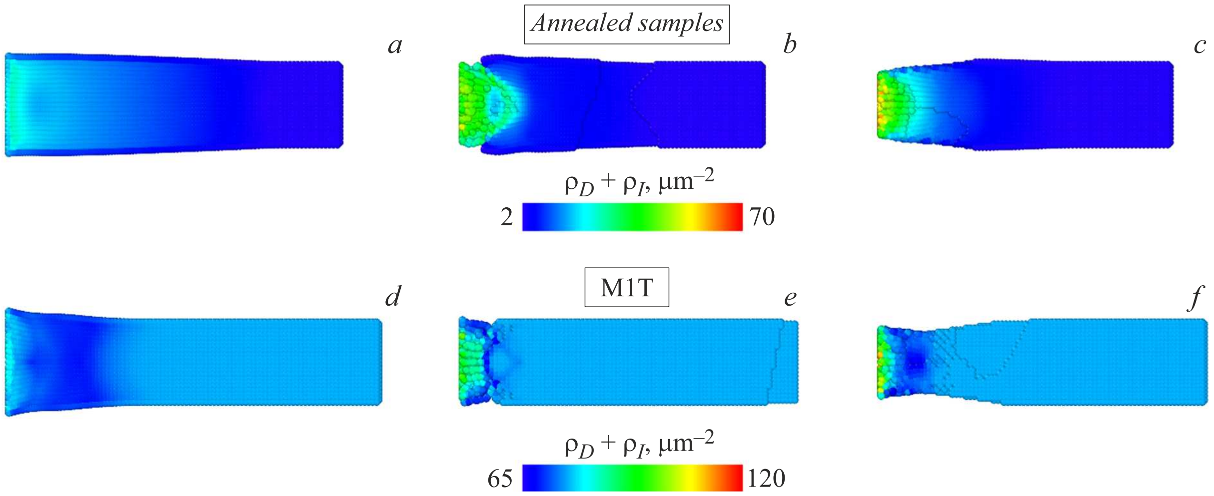

Figure 14. Total densities of dislocations in the annealed (a, b, c) and cold-rolled (d, e, f) copper at the moment of sample stopping for: *a, d* — conventional 8-mm cylinders; *b, e* — profiled 4-mm cylinders; *c, f* — truncated cones. The dislocation density at the back end of the bar corresponds to the initial state.

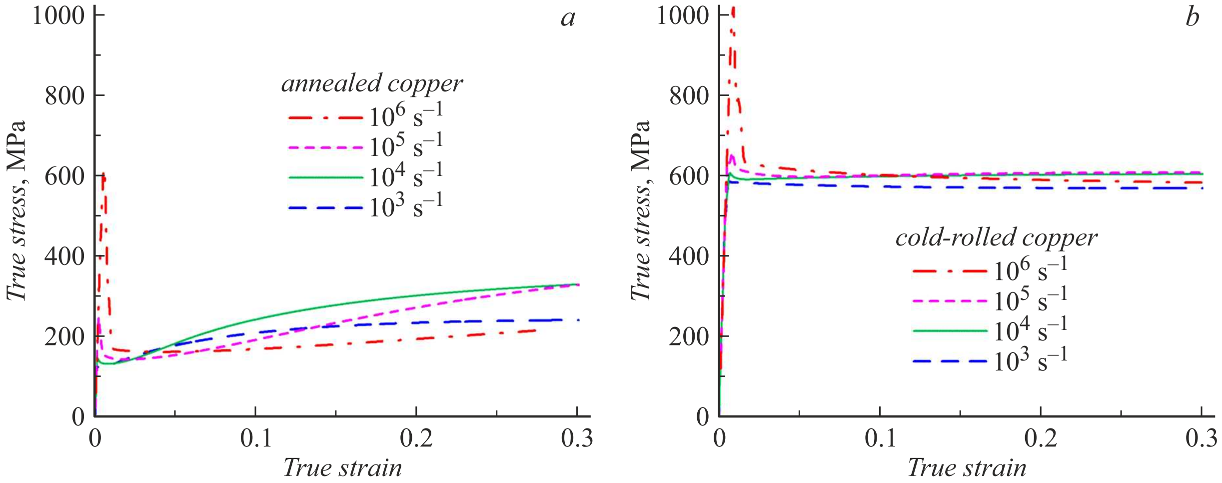

Figure 15. Strain–stress curves for: *a* — annealed copper; *b* — cold-rolled copper at strain rates of 10^3, 10^4, 10^5 and 10^6 s^{-1}, calculated according to dislocation-based plasticity model.

computation repeats the tendency of grain size refinement over a longer length compared to the cold-rolled samples. The thickness of the refined grains area is also well consistent with the experiment.

Conclusion

1. Experimental and numerical studies of the deformation of soft annealed copper impactors have been carried out and compared with the results from the previous study [19] for hard cold-rolled copper. The calculated and experimental data on changes in the size and shape of samples, as well as grain refinement under dynamic deformation, are compared.

2. Dislocation-based plasticity model [12] in a three-dimensional formulation [13], parameterized in [19] for cold-rolled copper, successfully describes the deformation of soft annealed copper when the initial density of immobile dislocations decreases to a level corresponding to annealed metals, which is a physically sound approach. Other model parameters were taken the same as for the cold-rolled copper.

3. For soft annealed impactors, the reduction in length and, hence, the degree of deformation is greater than for the hard cold-rolled ones, while plastic deformation itself is more evenly distributed along the length of the sample, while in samples of cold-rolled copper it is localized in the head.

4. The difference in nature of deformation of soft and hard copper can be explained from numerical studies by monotonous hardening of soft copper and partial deformational loss of strength of hard copper due to the annihilation

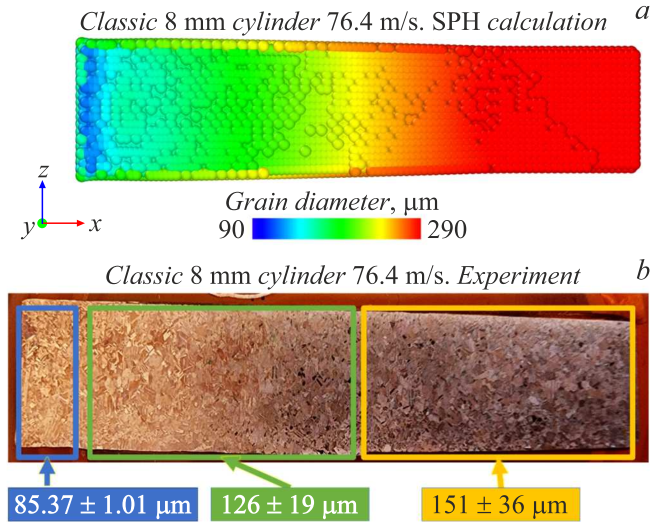

Figure 16. Calculated grain size in the annealed copper impactor for a 8-mm cylinder at impact velocity of 76.4 m/s (*a*) compared to experimental data (*b*).

of dislocations, which leads to the localization of plastic deformation in hard copper.

Funding

This study was supported by a grant from the Russian Science Foundation (project No. 20-11-20153-P), https://rscf.ru/project/23-11-45024/.

Conflict of interest

The authors declare that they have no conflict of interest.

References

[1] G.K. Johnson, W.H. Cook. In Proceedings of the 7th International Symposium on Ballistics, The Hague, 19–21, 1983.

[2] K.R.S. Vasu, Y.G. Vinith, S.G. Uday, G. Suneesh, M.B. Krishna. Mater. Today Proc, **62** (6), (2022). DOI: 10.1016/j.matpr.2022.04.279

[3] F.J. Zerilli, R.W. Armstrong. J. Appl. Phys., **61**, 1987. DOI: 10.1063/1.338024

[4] R.W. Armstrong, W. Arnold, F.J. Zerilli. Metall. Mater. Trans. A, **38**, 2007. DOI: 10.1007/s11661-007-9142-5

[5] D.L. Preston, D.L. Tonks, D.C. Wallace. J. Appl. Phys., **93** (1), (2003). DOI: 10.1063/1.1524706

[6] J.D. Colvin, R.W. Minich, D.H. Kalantar. Int. J. Plast., **25**, (2009). DOI: 10.1016/j.ijplas.2008.12.008

[7] R.A. Austin, D.L. McDowell. Int. J. Plast., **27**, (2011). DOI: 10.1016/j.ijplas.2010.03.002

[8] N.R. Barton, J.V. Bernier, R. Becker, A. Arsenlis, R. Cavallo, J. Marian, M. Rhee, H.-S. Park, B.A. Remington, R.T. Olson. J. Appl. Phys., **109**, (2011). DOI: 10.1063/1.3553718

[9] D.J. Luscher, J.R. Mayeur, H.M. Mourad, A. Hunter, M.A. Kenamond. Int. J. Plast., **76**, (2016). DOI: 10.1016/j.ijplas.2015.07.007

[10] S. Yao, X. Pei, J. Yu, Q. Wu. Int. J. Plast., **158**, (2022). DOI: 10.1016/j.ijplas.2022.103434

[11] V.S. Krasnikov, A.E. Mayer, A.P. Yalovets. Int. J. Plast., **27**, (2011). DOI: 10.1016/j.ijplas.2011.02.008

[12] A.E. Mayer, K.V. Khishchenko, P.R. Levashov, P.N. Mayer. J. Appl. Phys., **113**, (2013). DOI: 10.1063/1.4805713

[13] E.S. Rodionov, V.G. Lupanov, N.A. Grachyova, P.N. Mayer, A.E. Mayer. Metals, **12**, (2022). DOI: 10.3390/met12020264

[14] A.E. Mayer, V.S. Krasnikov, V.V. Pogorelko. Int. J. Plast., **139**, (2021). DOI: 10.1016/j.ijplas.2021.102953

[15] N.A. Gracheva, M.V. Lekanov, A.E. Mayer, E.V. Fomin. Mech. Solids., **3**, (2021). DOI: 10.31857/S0572329921020082

[16] D.J. Walters, A. Biswas, E.C. Lawrence, D.C. Francom, D.J. Luscher, D.A. Fredenburg, K.R. Moran, C.M. Sweeney, R.L. Sand-berg, J.P. Ahrens, C.A. Bolme. J. Appl. Phys., **124** (20), (2018). DOI: 10.1063/1.5051442

[17] T. Nguyen, D.C. Francom, D.J. Luscher, J.W. Wilkerson. J. Mech. Phys. Solids., **149**, (2021). DOI: 10.1016/j.jmps.2020.104284

[18] D. Rivera, J. Bernstein, K. Schmidt, A. Muyskens, M. Nelms, N. Barton, A. Kupresanin, J. Florando. Comput. Mater. Sci., **210**, (2022). DOI: 10.1016/j.commatsci.2021.110999

[19] E.S. Rodionov, V.V. Pogorelko, V.G. Lupanov, P.N. Mayer, A.E. Mayer. Materials, **16** (16), (2023). DOI: 10.3390/ma16165602

[20] V.V. Pogorelko, A.E. Mayer, E.V. Fomin, E.V. Fedorov. Int. J. Mech. Sci., **265**, (2024). DOI: 10.1016/j.ijmecsci.2023.108912

[21] K. Frydrych, M. Tomczak, S. Papanikolaou. Materials, **17**, (2024). DOI: 10.3390/ma17143397

[22] J. Halamka, M. Bartošák. Eng. Comput., in press, 2024. DOI: 10.1108/EC-02-2024-0166

[23] S.A. Zelepugin, R.O. Cherepanov, N.V. Pakhnutova. Materials, **16** (15), (2023). DOI: 10.3390/ma16155452

[24] D.A. Bilalov, M.A. Sokovikov, V.V. Chudinov, V.A. Oborin, Y.V. Bayandin, A.I. Terekhina, O.B. Naimark. J. Appl. Mech. Tech. Phys., **59** (7), (2018). DOI: 10.1134/S0021894418070027

[25] T. Nguyen, S.J. Fensin, D.J. Luscher. Int. J. Plast., **139**, (2021). DOI: 10.1016/j.ijplas.2021.102940

[26] Y.-M. Jeong, S. Hong, J.Y. Won, C. Kim, M.-G. Lee. Metals Mater. Intern., **30** (8), (2024). DOI: 10.1007/s12540-024-01636-6

[27] T. Antoun, L. Seaman, D.R. Curran, G.I. Kanel, S.V. Razorenov, A.V. Utkin. *Spall Fracture* (Springer, NY., 2003)

[28] G.I. Kanel, V.E. Fortov, S.V. Razorenov. Phys. Usp., **50**, (2007). DOI: 10.1070/PU2007v050n08ABEH006327

[29] L.M. Barker, R.E. Hollenbach. J. Appl. Phys., **43** (11), (1972). DOI: 10.1063/1.1660986

[30] G.I. Kanel, S.V. Razorenov, K. Baumung, J. Singer. J. Appl. Phys., **90**, (2001). DOI: 10.1063/1.1374478

[31] J.M. Winey, B.M. LaLone, P.B. Trivedi, Y.M. Gupta. J. Appl. Phys., **106**, (2009). DOI: 10.1063/1.3236654

[32] B. Gurrutxaga-Lerma, M.A. Shehadeh, D.S. Balint, D. Dini, L. Chen, D.E. Eakins. Int. J. Plast., **96**, (2017). DOI: 10.1016/j.ijplas.2017.05.001

[33] N.V. Saveleva, Y.V. Bayandin, A.S. Savinykh, G.V. Garkushin, S.V. Razorenov, O.B. Naimark. Tech. Phys. Lett., **44**, (2018). DOI: 10.1134/S1063785018090286

[34] S.F. Gnyusov, V.P. Rotshtein, A.E. Mayer, V.V. Rostov, A.V. Gunin, K.V. Khishchenko, P.R. Levashov. Int. J. Fract., **199**, (2016). DOI: 10.1007/s10704-016-0088-8

[35] S.F. Gnyusov, V.P. Rotshtein, A.E. Mayer, E.G. Astafurova, V.V. Rostov, A.V. Gunin, G.G. Maier. J. Alloys. Compd., **714**, (2017). DOI: 10.1016/j.jallcom.2017.04.219

[36] K. Baumung, H.J. Bluhm, B. Goel, P. Hoppé, H.U. Karow, D. Rusch, V.E. Fortov, G.I. Kanel, S.V. Razorenov, A.V. Utkin, O.Yu. Vorobjev. Laser Part. Beams, **14**, (1996). DOI: 10.1017/S0263034600009939

[37] K. Baumung, H. Bluhm, G.I. Kanel, G. Müller, S.V. Razorenov, J. Singer, A.V. Utkin. Int. J. Impact. Eng., **25**, (2001). DOI: 10.1016/S0734-743X(01)00004-5

[38] E. Moshe, S. Eliezer, E. Dekel, A. Ludmirsky, Z. Henis, M. Werdiger, I.B. Goldberg. J. Appl. Phys., **83**, (1998). DOI: 10.1063/1.367222

[39] I.K. Krasyuk, P.P. Pashinin, A.Y. Semenov, K.V. Khishchenko, V.E. Fortov. Laser Phys., **26**, (2016). DOI: 10.1088/1054-660X/26/9/094001

[40] S.I. Ashitkov, P.S. Komarov, E.V. Struleva, M.B. Agranat, G.I. Kanel. JETP Lett., **101**, (2015). DOI: 10.1134/S0021364015040049

[41] G.I. Kanel, E.B. Zaretsky, S.V. Razorenov, S.I. Ashitkov, V.E. Fortov. Phys. Usp., **60**, (2017). DOI: 10.3367/UFNe.2016.12.038004

[42] B. Zuanetti, S.D. McGrane, C.A. Bolme, V. Prakash. J. Appl. Phys., **123**, (2018). DOI: 10.1063/1.5027390

[43] W. Moćko, J. Janiszewski, J. Radziejewska, M. Grazka. Int. J. Impact. Eng., **75**, (2015). DOI: 10.1016/j.ijimpeng.2014.08.015

[44] N.V. Pakhnutova, E.N. Boyangin, O.A. Shkoda, S.A. Zelepugin. Adv. Eng. Res., **22**, (2022). DOI: 10.23947/2687-1653-2022-22-3-224-231

[45] S.A. Zelepugin, N.V. Pakhnutova, O.A. Shkoda, E.N. Boyangin. Metals, **12**, (2022). DOI: 10.3390/met12122186

[46] J. Xu, Q. Liu, Y.F. Xu, S.H. Guo, C. Li, N.B. Zhang, Y. Cai, X.Y. Liu, L. Lu, S.N. Luo. J. Alloys Compd., **936**, (2023). DOI: 10.1016/j.jallcom.2022.168261

[47] R.A. Gingold, J.J. Monaghan. Mon. Not. R. Astron. Soc., **181**, (1977). DOI: 10.1093/mnras/181.3.375

[48] J.J. Monaghan. Rep. Prog. Phys., **68**, (2005). DOI: 10.1088/0034-4885/68/8/R01

[49] J.J. Monaghan. Comput. Phys. Commun., **48**, (1998). DOI: 10.1016/0010-4655(88)90026-4

[50] A.E. Mayer, E.S. Rodionov, V.V. Pogorelko, P.N. Mayer. Chelyabinsk Phys. Math. J. 2025. in press.

[51] G.A. Merkulova. *Metallovedenie i termicheskaya obrabotka tsvetnykh splavov*: guide book (Siberian Federal University, Krasnoyarsk, 2008)

[52] N.V. Skripnyak, V.A. Skripnyak. *VII European Congress on Computational Methods in Applied Sciences and Engineering* (2016). DOI: 10.7712/100016.1818.11099

[53] V.F. Kuropatenko. J. Eng. Phys. Thermophys., **84**, (2011). DOI: 10.1007/s10891-011-0457-0

[54] D. Rittel, L.H. Zhang, S. Osovski. J. Mech. Phys. Solids., **107**, (2017). DOI: 10.1016/j.jmps.2017.06.016

[55] L.D. Landau, E.M. Lifshitz. *Theory of Elasticity; Course of Theoretical Physics* (Elsevier, Amsterdam, The Netherlands, **7**, 1986)

[56] J.P. Hirth, J. Lothe. *Theory of Dislocations* (Wiley & Sons, NY., USA, 1982)

[57] M. Peach, J.S. Koehler. Phys. Rev., **80**, (1950). DOI: 10.1103/PhysRev.80.436

[58] A.E. Dudorov, A.E. Mayer. Vestnik Chelyabinskogo gos. un-ta, **39** (254), (2011).

[59] V.S. Krasnikov, A.E. Mayer. Int. J. Plast., **101**, (2018). DOI: 10.1016/j.ijplas.2017.11.002

[60] K.V. Khishchenko, A.E. Mayer. Int. J. Mech. Sci., **189**, (2021). DOI: 10.1016/j.ijmecsci.2020.105971

[61] V.V. Bulatov, B.W. Reed, M. Kumar. Acta Mater., **65**, (2014). DOI: 10.1016/j.actamat.2013.10.057

[62] G. Zhou, Q. Huang, Y. Chen, X. Yu, H. Zhou. Metals, **12**, (2022). DOI: 10.3390/met12030451

[63] E.V. Fomin. Metals, **14** (4), (2024). DOI: 10.3390/met14040415

[64] J. Han, V. Vitek, D.J. Srolovitz. Acta Mater., **104**, (2016). DOI: 10.1016/j.actamat.2015.11.035

[65] S. Marrone, A. Di Mascio, D. Le Touzé. J. Comput. Phys., **310**, (2016). DOI: 10.1016/j.jcp.2015.11.059

[66] A. Stukowski. Modell. Simul. Mater. Sci. Eng., **18**, (2010). DOI: 10.1088/0965-0393/18/1/015012. http://www.ovito.org

[67] A.E. Mayer, V.S. Krasnikov. *ICTAEM 2019. In Proceedings of the Second International Conference on Theoretical, Applied and Experimental Mechanics* (Corfu, Greece, 23–26 June 2019, Springer, Manhattan, NY., USA, **8**, 2019) DOI: 10.1007/978-3-030-21894-2_12

[68] G.I. Kanel, A.S. Savinykh, G.V. Garkushin, S.V. Razorenov. J. Appl. Phys., **128** (11), (2020). DOI: 10.1063/5.0021212

[69] E.S. Rodionov, A.E. Mayer. Chelyabinsk Phys. Math. J., **8** (3), 399. DOI: 10.47475/2500-0101-2023-8-3-399-409

[70] I.A. Bryukhanov. Int. J. Plast., **165**, (2023). DOI: 10.1016/j.ijplas.2023.103599

[71] X. Wu, X. Wang, Y. Wei, H. Song, C. Huang. Int. J. Impact. Eng. **69**, (2014). DOI: 10.1016/j.ijimpeng.2014.02.016

[72] M.A. Meyers, U.R. Andrade, A.H. Chokshi. Metall. Mater. Trans. A, **26A**, (1995).

Translated by T.Zorina

Translated by T.Zorina